Boundary-Layer Meteorol (2010) 137:135–152
DOI 10.1007/s10546-010-9520-1

ARTICLE

A Lagrangian Stochastic Model for Sea-Spray Evaporation in the Atmospheric Marine Boundary Layer

James Mueller · Fabrice Veron

Received: 2 November 2009 / Accepted: 11 June 2010 / Published online: 6 July 2010

Abstract The dispersion of heavy particles subjected to a turbulent forcing is often simulated with Lagrangian stochastic models. Although these models have been employed successfully over land, the implementation of traditional LS models in the marine boundary layer is significantly more challenging. We present an adaptation of traditional Lagrangian stochastic models to the atmospheric marine boundary layer with a particular focus on the representation of the scalar turbulence for temperature and humidity. In this new model, the atmosphere can be stratified and the bottom boundary is represented by a realistic wavy surface that moves and deforms. Hence, the correlation function for the turbulent flow following a particle is extended to the inhomogenous, anisotropic case. The results reproduce behaviour for scalar Lagrangian turbulence in a stratified airflow that departs only slightly from the expected behaviour in isotropic turbulence. When solving for the surface temperature and the radius of evaporating heavy water droplets in the airflow, the modelled turbulent forcing on the particle also behaves remarkably well. We anticipate that this model will prove especially useful in the context of sea-spray dispersion and its associated sensible heat, latent heat, and gas fluxes between spray droplets and the atmosphere.

Keywords Lagrangian stochastic model · Marine boundary layer · Multiphase flow · Sea-spray evaporation

1 Introduction

The sensible heat and water vapour fluxes at the air–sea interface are important boundary conditions for atmospheric and oceanic numerical models that attempt to capture the physics

J. Mueller · F. Veron (✉)
School of Marine Science and Policy, College of Earth, Ocean and Environment, University of Delaware, 112C Robinson Hall, Newark, DE 19716, USA
e-mail: fveron@udel.edu

J. Mueller
e-mail: jmueller@udel.edu

and evolution of weather and climate. While these fluxes are fairly well-known at moderate wind speeds, they remain obscured at high wind speeds found in storms and hurricanes. In high wind-speed conditions, frequent wave-breaking along with airflow and surface separation produce sea spray in the air and these spray droplets are believed to significantly influence the heat and water vapour fluxes between the ocean and the atmosphere. However, accurate estimates of the spray-mediated fluxes depend on a robust description of the trajectories, temperature and size evolution of the spray droplets as they are transported in the near surface, turbulent atmospheric marine boundary layer (MBL).

The study of small particle dispersion and evolution in any boundary layer inherently involves the study of turbulence, since molecular diffusion is orders of magnitude smaller than turbulent diffusion. Because direct numerical simulation techniques are too computationally expensive for most applications, including that presented here, the turbulent flow needs to be modelled. Different turbulence models have various strengths and weaknesses, and the results can be sensitive to the model that is used. For this study, we choose to use a Lagrangian turbulence model. Although Lagrangian coordinates, which follow the trajectories of individual fluid parcels, are sometimes more physically intuitive in describing fluid motion than Eulerian coordinates that are fixed in space, Lagrangian coordinates are used less frequently because they are often awkward to implement. Studies of particle dispersion, however, are well-suited to a Lagrangian frame of reference (Yeung 2002), and modern computing power has enabled the calculation of the large number of random trajectories necessary for Lagrangian stochastic (LS) modelling. A primary advantage is the superior accuracy of dispersion simulation in the near field of a source. Recent advances in LS models for heavy particle dispersion in the marine boundary layer above a complex unsteady bottom boundary, and where the turbulence is anisotropic and inhomogenous (Mueller and Veron 2009b), have been rather encouraging and motivate the work presented here.

For the scalar fields such as temperature and water vapour, the advantage of LS models lies in their ability to include temporal evolution of the particle phase, such as droplet evaporation, with relative ease. An important drawback, however, is the difficulty involved in the calculation of the ambient scalar fields surrounding a moving heavy particle. The fluid temperature and humidity at the particle location do not follow that of a Lagrangian massless fluid particle. Therefore, we also formulate in this paper a hybrid of the Eulerian and Lagrangian (spatial and temporal) frames of reference.

Unfortunately, Lagrangian turbulence models for passive scalars are still relatively unsophisticated when compared to their velocity analogue, and the LS model presented here for both temperature and water vapour differs substantially from our recent advances with regard to velocity (Mueller and Veron 2009b).

2 Scalar Mean and Turbulence Profiles

To model the instantaneous temperature and specific humidity of the airflow in the MBL and above a wavy surface, we use the standard Reynolds decomposition where the potential temperature and specific humidity of the air, θ and q, respectively, are represented by

$$\theta = \Theta + \theta', \tag{1a}$$

$$q = Q + q'. \tag{1b}$$

Here Θ and Q are the ensemble (or temporal) averages in surface-following coordinates, and θ' and q' are the turbulent deviations from the respective means. Similarly, the air velocity is decomposed into:

$$u_i = U_i + u_i', \tag{2}$$

where, in this model, we only consider the vertical and streamwise horizontal directions, i.e. $i = \{1, 3\}$ (see Mueller and Veron 2009b, for details).

2.1 Eulerian Mean

Following the decomposition above, we first examine the mean temperature and humidity. Turbulent boundary-layer theory over a smooth flat surface offers a starting point for the mean scalar profile over ocean waves. Within a turbulent boundary layer, we consider two distinct regions. The first region closest to the surface is the diffusive sublayer, where molecular effects dominate, and the scalar profile in this layer is linear. The second region is the logarithmic layer, where the turbulent fluxes dominate and the scalar profile becomes logarithmic. In smooth flow, these two regions are self-similar in wall coordinates (i.e. normalized distance from the wall $z^+ = zu_*/\nu$, where u_* is the friction velocity and ν is the kinematic viscosity of the air). In the MBL, waves form, grow, and interact. Small capillary waves effectively cause the surface to become rougher, and surface gravity waves make the surface topographically uneven. In addition, the waves propagate at different phase speeds. Therefore, the velocity profile over ocean waves, not surprisingly, departs from the smooth, flat plate case, and these effects on the momentum flux also translate to a departure from smooth flow for the scalar fluxes (Mueller and Veron 2009c). The partition of the surface stress is modelled according to Mueller and Veron (2009a), while the details of the scalar flux partitions at the surface are described in Mueller and Veron (2009c). The finer points of the scalar flux profiles, however, will be described in the next section.

The form for the mean temperature and humidity profiles is determined using a hybrid of the standard logarithmic profile from flat plate theory and the van Driest damping function (van Driest 1956), which approximates both the near-wall linear, molecular sublayer and the smooth transition to the logarithmic layer. In fact, the mean scalar profile is simply the summation of the two layers with the logarithmic layer exponentially damped in the near-wall region. In wave-following coordinates (where the height above the surface is denoted by ζ), and assuming constant-flux layers, the mean velocity profile is analogous to that presented in Mueller and Veron (2009a, b) and can be written using the notation given in Liu et al. (1979) for comparison:

$$\begin{aligned} U(\zeta) - U_0 = {} & Cu_{*_\nu}\left(1 - \exp(-\zeta u_*/C\nu)\right)\left|\frac{u_{*_\nu}}{u_*}\right| \\ & + \frac{u_*}{\kappa}\left[\ln\left(\frac{\zeta+\delta}{\delta}\right) - \Phi_m\right]\left(1 - \exp(-\zeta u_*/C\nu)\right), \end{aligned} \tag{3}$$

where C is the viscous layer height in wall coordinates and usually taken to be $O(10)$. The equivalent temperature and humidity mean profiles become (Mueller and Veron 2009c):

$$\begin{aligned} \Theta(\zeta) - \Theta_0 = {} & S\theta_*\left(1 - \exp(-\zeta u_*/SK_\theta)\right)\left|\frac{u_{*_\nu}}{u_*}\right| \\ & + \frac{\theta_*}{\kappa}\left[\ln\left(\frac{\zeta+\delta_\theta}{\delta_\theta}\right) - \Phi_\theta\right]\left(1 - \exp(-\zeta u_*/SK_\theta)\right), \end{aligned} \tag{4a}$$

$$\begin{aligned} Q(\zeta) - Q_0 = {} & Dq_*\left(1 - \exp(-\zeta u_*/DK_q)\right)\left|\frac{u_{*_\nu}}{u_*}\right| \\ & + \frac{q_*}{\kappa}\left[\ln\left(\frac{\zeta+\delta_q}{\delta_q}\right) - \Phi_q\right]\left(1 - \exp(-\zeta u_*/DK_q)\right), \end{aligned} \tag{4b}$$

where $\kappa = 0.4$ is the von Karman constant, $\rho u_{*_\nu}^2$ represents the viscous component of the total surface stress ρu_*^2, and ρ denotes the air density, θ_* and q_* are the turbulent scales for sensible heat and water vapour, respectively, and θ_0 and q_0 are the corresponding surface values. Also, K_θ and K_q are the diffusivities for heat and water vapour respectively, S and D are the heights of the molecular layers in wall coordinates, and relate to the viscous sublayer thickness C with $S = CPr^{1/2}$ and $D = CSc^{1/2}$, where $Pr = \nu/K_\theta$ and $Sc = \nu/K_q$ are respectively the Prandtl (≈ 0.72 at 20°C) and Schmidt (≈ 0.63 at 20°C) numbers. The stability corrections due to stratification, $\Phi_\theta(\zeta/L)$ and $\Phi_q(\zeta/L)$, are a function of the height, ζ, and the Obukhov length scale, L. The variables δ_θ and δ_q merely ensure a smooth transition between the two layers, regardless of the flow roughness. The profile form given in Eq. 4 offers a continuous (and second-order differentiable) formulation that smoothly connects the molecular (linear) and logarithmic layers. The van Driest components have been slightly modified to account for the roughness of the flow. The profiles converge to the habitual surface limits (i.e. $\zeta^+ \to 0$), and yield $(\Theta - \Theta_0)/\theta_* = Pr\zeta^+ \left|u_{*_\nu}/u_*\right|$ and $(Q - Q_0)/q_* = Sc\zeta^+ \left|u_{*_\nu}/u_*\right|$. In the smooth flow limit where the surface stress is entirely due to viscosity, the surface limits further reduce to $(\Theta - \Theta_0)/\theta_* = Pr\zeta^+$ and $(Q - Q_0)/q_* = Sc\zeta^+$. Accordingly, the kinematic molecular fluxes at the surface are $K_\theta d\Theta/d\zeta|_{\zeta=0} = \theta_* \left|u_{*_\nu}\right|$ and $K_q dQ/d\zeta|_{\zeta=0} = q_* \left|u_{*_\nu}\right|$. Outside the molecular sublayers, the profiles converge to the non-singular, standard logarithmic layers with

$$\Theta(\zeta) - \Theta_0 = \frac{\theta_*}{\kappa}\left[\ln\left(\frac{\zeta + \delta_\theta}{z_\theta}\right) - \Phi_\theta\right], \tag{5a}$$

$$Q(\zeta) - Q_0 = \frac{q_*}{\kappa}\left[\ln\left(\frac{\zeta + \delta_q}{z_q}\right) - \Phi_q\right]. \tag{5b}$$

The roughness lengths z_θ and z_q are given by

$$\delta_\theta = z_\theta \exp\left(\kappa S \left|\frac{u_{*_\nu}}{u_*}\right|\right), \tag{6a}$$

$$\delta_q = z_q \exp\left(\kappa D \left|\frac{u_{*_\nu}}{u_*}\right|\right). \tag{6b}$$

As they follow the surface displacement, the mean temperature and water vapour profiles are shifted up and down, with the wave-following vertical coordinate ζ simply the distance above the local surface, $\zeta(x, z, t) = z - \eta(x, t)$, where $\eta(x, t)$ is the instantaneous wavy water surface. We choose to follow the empirical omni-directional spectrum of Elfouhaily et al. (1997) to describe the amplitudes of capillary and deep-water gravity wave modes, a_n, but any other spectrum can be substituted. The instantaneous elevation of the surface is then estimated as a linear superposition of these modes and becomes:

$$\eta(x, t) = \sum_n a_n \cos\left(k_n x - \omega_n t + \phi_n\right), \tag{7}$$

where k_n, ω_n, and ϕ_n are the wavenumber, orbital frequency, and phase of each wave mode n respectively. The phase speed of each wave mode is $c_n = \omega_n/k_n$, determined by the dispersion relationship for deep-water capillary-gravity waves. Each wave phase, ϕ_n, is chosen from a random distribution uniformly distributed on the interval $[-\pi, \pi)$.

2.2 Lagrangian Stochastic Scalar Turbulence

Once the mean scalar fields are determined, the turbulent deviation needs to be modelled. The underlying principle of Lagrangian stochastic (LS) models is that certain variables of a fluid

particle evolve as a Markov process, which means that consecutive values in time are only partially correlated and the uncorrelated component is independent of previous values (for a review of LS models, see Rodean 1996). For the fluid kinematics, Markov processes are not only well understood mathematically but can also be used to describe the evolution of the position, velocity, and acceleration of a fluid element within a turbulent flow. A zero-order LS model treats the fluid particle position as Markovian, and the random displacement model is recovered. Likewise, a first-order LS model, or originally proposed by Taylor (1921) as the drunkard's walk, treats the fluid particle velocity as Markovian, thereby recovering the generalized Langevin equation (Thomson 1987). Finally, a second-order LS model treats the acceleration as Markovian (Du et al. 1995). For the scalar turbulent components of a fluid particle, we consider here a model similar to a Langevin-type evolution:

$$d\theta' = a_\theta dt + b_{\theta u_3} d\xi_{u_3} + b_\theta d\xi_\theta, \tag{8a}$$

$$dq' = a_q dt + b_{q u_3} d\xi_{u_3} + b_q d\xi_q, \tag{8b}$$

where $d\xi_{u_3}$, $d\xi_\theta$ and $d\xi_q$ are independent Gaussian variables with zero mean and variance dt. The natural approach to modelling a_θ and a_q would be to extend the drift term from the Lagrangian stochastic model of velocity (see Mueller and Veron 2009b) by substituting θ and q and eliminating dimensionally incorrect terms. This approach, however, does not reproduce the correct second-order, one-point correlations ($\overline{\theta'^2}$, $\overline{q'^2}$, $\overline{u_3'\theta'}$ and $\overline{u_3'q'}$).

Recent work comparing Lagrangian stochastic models of passive scalars to direct numerical simulations results is promising (Couzinet 2008), but ultimately such models are unable to recover the one-point correlations in more complicated flows such as that presented here. However, though the corresponding probability distribution function may not be exactly right, the one-point correlations can still be recovered if we instead follow an approach similar to Moissette et al. (2001). The model presented here applies the bulk stress model of Mueller and Veron (2009a) and solves the generalized Langevin equation for the fluid velocity, extending the Lagrangian stochastic model of the continuous phase fluid in Moissette et al. (2001) to the marine boundary layer, where the turbulence is non-homogenous. The current model also adapts the heavy particle correlation function from Mueller and Veron (2009b) and solves the full equation of motion and microphysical equations for the discrete phase fluid, extending the model to the case of evaporating sea-spray drops with significant inertia. Accordingly, the first terms in Eq. 8 follow the form of the classical Langevin equation:

$$a_\theta = -\frac{C_\theta \varepsilon_\theta}{\sigma_\theta^2}\theta' = -\frac{\theta'}{T_{L_\theta}}, \tag{9a}$$

$$a_q = -\frac{C_q \varepsilon_q}{\sigma_q^2} q' = -\frac{q'}{T_{L_q}}, \tag{9b}$$

where $C_\theta \approx \pi/2$ and $C_q \approx \pi/2$ are the constants from the second-order Lagrangian structure functions of temperature and water vapour, respectively, and ε_θ and ε_q are the respective scalar dissipation rates. The corresponding variances for the scalar turbulence are σ_θ^2 and σ_q^2. The specification of these scalar dissipation rates and integral time scales $T_{L_\theta} = \sigma_\theta^2 / C_\theta \varepsilon_\theta$ and $T_{L_q} = \sigma_q^2 / C_q \varepsilon_q$, will be presented in more detail below. The diffusion terms b_θ and b_q are similar to their velocity counterparts but are modified to ensure that the heat and water vapour fluxes, i.e. the covariances, are recovered:

$$b_\theta^2 = 2C_\theta \varepsilon_\theta \left(1 - \frac{\hat{H}_{\theta 3}^2}{\hat{H}_{\theta\theta}\hat{\tau}_{33}}\right), \tag{10a}$$

$$b_q^2 = 2C_q \varepsilon_q \left(1 - \frac{\hat{M}_{q3}^2}{\hat{M}_{qq}\hat{\tau}_{33}}\right), \tag{10b}$$

where $\hat{\mathbf{H}}$, $\hat{\mathbf{M}}$, and $\hat{\boldsymbol{\tau}}$ are, respectively, the normalized heat flux, water vapour flux, and stress tensors:

$$\hat{\mathbf{H}} = \begin{pmatrix} \hat{H}_{\theta\theta} & \hat{H}_{\theta 3} \\ \hat{H}_{3\theta} & \hat{H}_{33} \end{pmatrix}, \tag{11a}$$

$$\hat{\mathbf{M}} = \begin{pmatrix} \hat{M}_{qq} & \hat{M}_{q3} \\ \hat{M}_{3q} & \hat{M}_{33} \end{pmatrix}, \tag{11b}$$

and

$$\hat{\boldsymbol{\tau}} = \begin{pmatrix} \hat{\tau}_{11} & \hat{\tau}_{13} \\ \hat{\tau}_{31} & \hat{\tau}_{33} \end{pmatrix} \tag{11c}$$

whose components will be defined explicitly in the next section. The other Wiener process in Eq. 8 should evolve as the second-order Lagrangian structure function of (vertical) velocity and temperature or water vapour (Couzinet 2008), but to ensure that all second-order, one-point correlations are recovered, these terms are taken to be

$$b_{\theta u_3} = \sqrt{2C_\theta \varepsilon_\theta}\, \hat{H}_{\theta 3} / \sqrt{\hat{H}_{\theta\theta}\hat{\tau}_{33}}, \tag{12a}$$

$$b_{q u_3} = \sqrt{2C_q \varepsilon_q}\, \hat{M}_{q3} / \sqrt{\hat{M}_{qq}\hat{\tau}_{33}}. \tag{12b}$$

In discretized form, in which Δt is the numerical timestep, the temperature and water vapour fluctuations at time $t + \Delta t$ are

$$\theta'(t+\Delta t) = \theta'(t)\, R_\theta + \sigma_\theta \sqrt{1 - R_\theta^2} \left(\gamma_{u_3} \hat{H}_{\theta 3} / \sqrt{\hat{H}_{\theta\theta}\hat{\tau}_{33}} + \gamma_\theta \sqrt{1 - \frac{\hat{H}_{\theta 3}^2}{\hat{H}_{\theta\theta}\hat{\tau}_{33}}}\right), \tag{13a}$$

$$q'(t+\Delta t) = q'(t)\, R_q + \sigma_q \sqrt{1 - R_q^2} \left(\gamma_{u_3} \hat{M}_{q3} / \sqrt{\hat{M}_{qq}\hat{\tau}_{33}} + \gamma_q \sqrt{1 - \frac{\hat{M}_{q3}^2}{\hat{M}_{qq}\hat{\tau}_{33}}}\right), \tag{13b}$$

where $R_\theta = \exp\left(-\Delta t / T_{L_\theta}\right)$ and $R_q = \exp\left(-\Delta t / T_{L_q}\right)$ are the autocorrelation functions of temperature and water vapour, respectively. Finally, γ_{u_3}, γ_θ, and γ_q are independent Gaussian variables with zero mean and unit variance.

As noted earlier, the scalar fields and the description of the mean and turbulent quantities are linked to the description of the velocity and stresses in the MBL. For the work presented here, we have used our previous parameterizations for the air–sea stress (Mueller and Veron 2009a), and for the air–sea scalar fluxes (Mueller and Veron 2009c), but other models can be readily used instead. Similarly, the LS model for the temperature and humidity is dependant on a turbulence model for the velocity. For example $\hat{\boldsymbol{\tau}}$ is needed and γ_{u_3} is a Gaussian variable for the vertical turbulent velocity. To estimate these, we use here the Lagrangian stochastic model of Mueller and Veron (2009b) which has been specifically designed to include various phenomena found in the MBL such as wavy surfaces and atmospheric stratification.

With the Eulerian means and turbulent fluctuations described above, the (total) temperature and humidity at the location of a heavy particle such as a sea-spray droplet can be obtained. The heat and water vapour flux tensors above are the only remaining variable needed for the LS model.

3 Flux Profiles and Heavy Particle Autocorrelation

We briefly describe here the scalar flux model employed by Mueller and Veron (2009c), which was specifically developed in the context of the stratified MBL for looking at spray dispersion problems. The constant-flux assumption yields the profiles of sensible heat and water vapour fluxes[1]:

$$H(\zeta) = H(0) = H_{mol}(\zeta) + H_t(\zeta), \tag{14a}$$

$$M(\zeta) = M(0) = M_{mol}(\zeta) + M_t(\zeta), \tag{14b}$$

with respective molecular fluxes (H_{mol} and M_{mol}) and turbulent fluxes (H_t and M_t). Although the total fluxes are conserved, the fraction of each component changes away from the surface. The vertical profiles of the molecular fluxes are implicitly defined from the mean profiles, and under the assumption that the contribution from the wave perturbation is negligible, they can be approximated as:

$$H_{mol}(\zeta) \approx \rho c_p K_\theta \frac{\partial \Theta(\zeta)}{\partial \zeta}, \tag{15a}$$

$$M_{mol}(\zeta) \approx \rho K_q \frac{\partial Q(\zeta)}{\partial \zeta}. \tag{15b}$$

From the constant-flux assumption, the preceding two equations yield the turbulent flux profiles:

$$H_t(\zeta) = H(0) - H_{mol}(\zeta), \tag{16a}$$

$$M_t(\zeta) = M(0) - M_{mol}(\zeta). \tag{16b}$$

Figure 1a shows the vertical profiles in wall coordinate for the mean temperature (Eq. 4a) at three different 10-m wind speeds, with corresponding dominant wave slopes between 0.10 and 0.16. The vertical mean profiles for the moisture (not shown) are not significantly different. The effects of the surface waves on the mean profiles are not explicitly modelled and therefore play a role only in the modification of the turbulent friction velocity profiles (Mueller and Veron 2009c). Figure 1a indeed shows only a small difference in the mean heat profiles with increasing wind speeds and surface wave slopes. The corresponding molecular heat fluxes (Eq. 15a) normalized by the surface heat fluxes $H(0)$ are shown on Fig. 1b for the corresponding wind speeds. As expected, the maximum molecular flux fraction is attained within the molecular sublayer where $\zeta^+ \sim O(1-10)$. The decrease in the normalized molecular flux at the surface is a result of the flow roughness, airflow separation, and surface waves, which are acounted for in the stress model and yield a non-zero turbulent and wave induced fraction of the momentum flux at the surface (i.e. at the surface, the viscous stress $\rho u_{*_v}^2$ does not account for the total stress ρu_*^2). Therefore, at the surface, the molecular flux of heat is given by: $H_{mol}(0) = \rho c_p K_\theta d\Theta/d\zeta|_{\zeta=0} = \rho c_p \theta_* \left|u_{*_v}\right| < H(0) = \rho c_p \theta_* |u_*|$. Alternatively, this means that $H(0) \neq H_{mol}$ and $H_t(0) \neq 0$.

[1] The water vapour flux M relates to the commonly used latent heat flux E with $M = E/L_v$ where L_v the latent heat of evaporation.

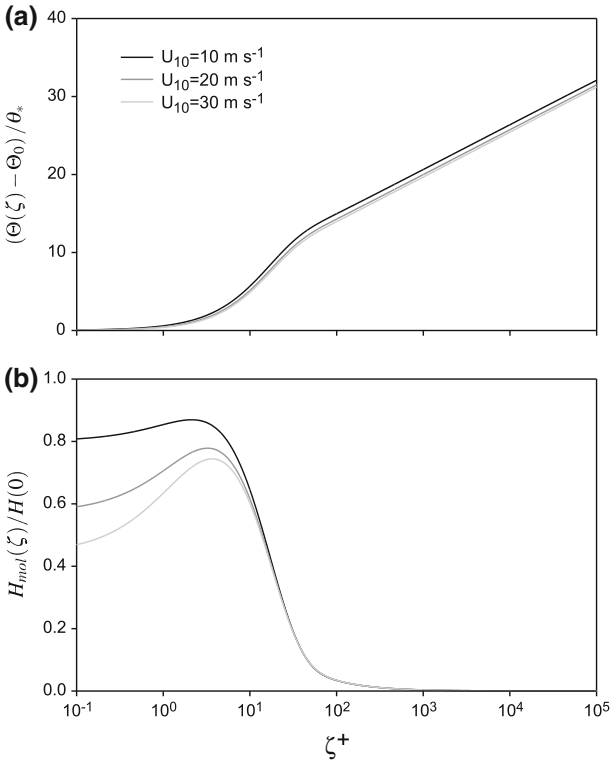

Fig. 1 (**a**) Vertical profiles of the mean temperature for 10-m wind speeds of 10 m s^{-1} (*black*), 20 m s^{-1} (*dark grey*), and 30 m s^{-1} (*light grey*); (**b**) the corresponding molecular heat flux (Eq. 15a), normalized by the fluxes at the surface

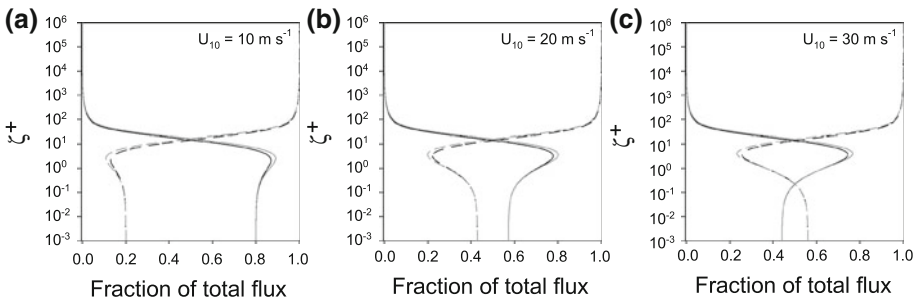

Fig. 2 Vertical profiles of the molecular (*solid line*) and nonmolecular (*dashed line*) flux fractions for heat (*black*) and water mass (*dark grey*) for 10-m wind speeds of 10 m s^{-1} (**a**), 20 m s^{-1} (**b**), and 30 m s^{-1} (**c**)

Figure 2 shows the vertical profiles of the scalar flux components for the three different 10-m wind speeds in Fig. 1. As the wind speed increases, the molecular fraction of the surface scalar fluxes decreases, while the non-molecular fractions of the scalar fluxes increase. The height of the molecular layer is nearly constant in wall coordinates for all wind speeds, though the heights for the heat and water mass fluxes are slightly different because the Prandtl number is unequal to the Schmidt number. Since we have not explicitly modelled the wave-induced components of the scalar fluxes, the non-molecular components of the scalar fluxes

are assumed to be turbulent throughout the boundary layer. Therefore, the non-molecular fluxes are hereafter considered to be turbulent fluxes.

With the turbulent flux constituents, the components of the heat and water vapour flux tensors from the previous section can now be defined as

$$\hat{H}_{\theta\theta} = \sigma_\theta^2, \tag{17a}$$

$$\hat{H}_{\theta 3} = -H_t/\rho c_p, \tag{17b}$$

and

$$\hat{M}_{qq} = \sigma_q^2, \tag{18a}$$

$$\hat{M}_{q3} = -M_t/\rho, \tag{18b}$$

and where the standard deviations of the turbulent scalars in neutral stratification conditions are:

$$\sigma_\theta = 2.9 H_t/\rho c_p u_* = 2.9\theta_*, \tag{19a}$$

$$\sigma_q = 2.9 M_t/\rho u_* = 2.9 q_*. \tag{19b}$$

Assuming that dissipation equals production, a fair assumption except in extremely stratified flows (Edson and Fairall 1998), the mean dissipation rates for the temperature and water vapour variances can be respectively expressed as

$$\varepsilon_\theta = -2\overline{u_3'\theta'}\frac{d\Theta}{d\zeta} = \frac{2H_t}{\rho c_p}\frac{d\Theta}{d\zeta}, \tag{20a}$$

$$\varepsilon_q = -2\overline{u_3' q'}\frac{dQ}{d\zeta} = \frac{2M_t}{\rho}\frac{dQ}{d\zeta}. \tag{20b}$$

We note here that all of the terms in Eqs. 17–20 vary with height because the turbulent fluxes change with height.

This closes the LS model of scalars for fluid particles and fully defines the scalars that include a mean component and a Lagrangian turbulent fluctuation. In the context of investigating the Lagrangian dispersion of heavy particles, however, the LS model needs to be further extended to non-fluid particles, whose trajectories differ from those of air parcels.

We propose a formulation that not only tracks the separation at each timestep explicitly but also extends to the anisotropic case, which is necessary to properly model the stratified MBL. When the turbulent intensity of velocity differs in the horizontal and vertical directions, there are two (streamwise horizontal, $i = 1$; and vertical, $i = 3$) Eulerian length scales for each scalar, temperature and water vapour:

$$L_{\theta_i} = \frac{\sigma_\theta^2 \sigma_i}{2\varepsilon_\theta}, \tag{21a}$$

$$L_{q_i} = \frac{\sigma_q^2 \sigma_i}{2\varepsilon_q}. \tag{21b}$$

The resulting two autocorrelation coefficients include both the Lagrangian time scale and Eulerian length scales as:

$$\hat{R}_\theta = \exp\left[-\frac{\Delta t}{T_{L_\theta}} - \left(\frac{|s_1|}{L_{\theta_1}}\right)^{\frac{2}{3}} - \left(\frac{|s_3|}{L_{\theta_3}}\right)^{\frac{2}{3}}\right], \tag{22a}$$

$$\hat{R}_q = \exp\left[-\frac{\Delta t}{T_{L_q}} - \left(\frac{|s_3|}{L_{q_3}}\right)^{\frac{2}{3}} - \left(\frac{|s_1|}{L_{q_1}}\right)^{\frac{2}{3}}\right], \tag{22b}$$

where **s** is the separation vector between the fluid particle trajectory and the heavy particle trajectory. Our model therefore differentiates the direction of the separation between the fluid particle and heavy particle at each timestep and calculates the decorrelation accordingly. Also, the exponent for the separation between the fluid particle and the heavy particle is 2/3, as given by the Eulerian structure function, instead of 1. The autocorrelation function (Eq. 22) satisfies both the limit of an extremely heavy particle falling through the turbulent eddies and that of a massless fluid particle following the turbulent eddies.

4 Droplet Microphysics

With the LS model complete, we can now evaluate the evolution of a droplet size and temperature as it evolves through the turbulent marine boundary layer. Following Andreas (1990, 1995) and Edson and Fairall (1994), the temporal evolution of the radius and temperature of a saline (NaCl) water droplet in air is given by

$$\frac{dr}{dt} = \frac{f_w K_q^{'} M_w e_s}{\rho_p r R\theta} \times \left[Q_{RH} - \frac{1}{1+\delta}\exp\left(\frac{L_v M_w}{R\theta}\frac{\delta}{1+\delta} + \frac{2M_w\Gamma}{R\theta\rho_w r\,(1+\delta)} + \frac{I\Phi_s m_s\,(M_w/M_s)}{\left(4\pi r^3\rho_p/3\right) - m_s}\right)\right], \tag{23}$$

$$\frac{dT_p}{dt} = \frac{-3}{r^2\rho_p c_{ps}}\left(f_h k_a'\left(\theta - T_p\right) + f_w L_v K_q'\left(\rho q - q_p\right)\right), \tag{24}$$

where Q_{RH} is the fractional relative humidity, ρ_p the particle density and ρ_w the pure water density, R is the universal gas constant, M_w and M_s are the molecular weights of water and salt, respectively, e_s is the saturation vapour pressure at the droplet temperature T_p, c_{ps} is the specific heat of salty water, L_v is the latent heat of vaporization, Γ is the surface tension for a flat surface, m_s is the mass of salt in the droplet, $I = 2$ is the number of ions salt dissociates into, ϕ_s is the osmotic coefficient, and $\delta = T_p/\theta - 1$. The ambient potential temperature and specific humidity for moist air, θ and q, are modelled as described above.

The water vapour density on the droplet surface is

$$q_p = \frac{M_w e_s}{R\theta}\exp\left(\frac{2M_w\Gamma}{R\theta\rho_w r\,(1+\delta)} + \frac{I\Phi_s m_s\left(M_w/M_s\right)}{\left(4\pi r^3\rho_p/3\right) - m_s}\right). \tag{25}$$

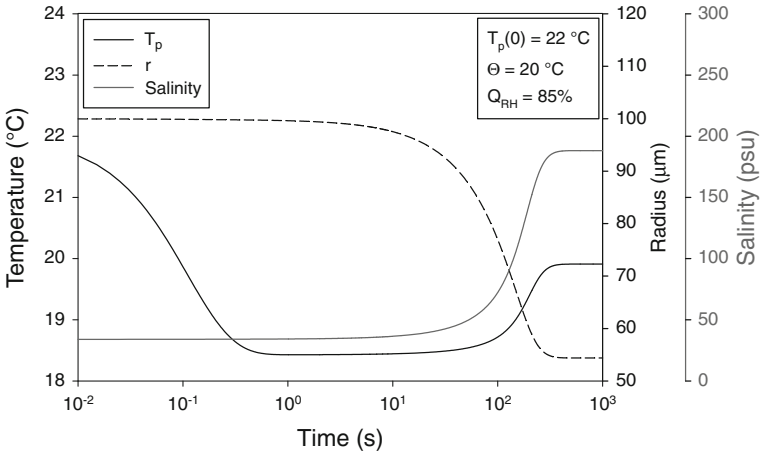

Fig. 3 Evolution of temperature (*solid*), radius (*dashed*) and salinity (*grey*) for a water droplet with initial radius 100 μm, initial temperature 22°C and initial salinity 34 psu

The modified diffusivity for water vapour, K_q', and the thermal conductivity of air, k_a', include non-continuum effects and are, respectively, given by

$$K_q^{'} = \frac{K_q}{\frac{r}{r+\delta_w} + \frac{K_q}{r\alpha_c}\left(\frac{2\pi M_w}{R\theta}\right)^{1/2}}, \tag{26}$$

$$k_a^{'} = \frac{k_a}{\frac{r}{r+\delta_T} + \frac{k_a}{r\alpha_T \rho_{ad} c_{pd}}\left(\frac{2\pi M_a}{R\theta}\right)^{1/2}}, \tag{27}$$

where K_q and k_a are the usual molecular diffusivity for water vapour and thermal conductivity of air, respectively, M_a is the molecular weight of dry air, c_{pd} and ρ_{ad} are respectively the specific heat and density for dry air, and with constants $\delta_w = 8 \times 10^{-8}$, $\alpha_c = 0.036$, $\delta_T = 2.16^{-7}$, and $\alpha_T = 0.7$. Ventilation coefficients $f_w = f_h = 1 + \sqrt{Re_p}/4$ are corrections to the heat and water vapour diffusivity for large instantaneous particle Reynolds numbers, i.e. $Re_p = 2r\,|\mathbf{u} - \mathbf{v}|/\nu \gg 1$, where the total velocity vector of the air is given by $\mathbf{u}$, while that of the particle is denoted by $\mathbf{v}$.

At each timestep, the model calculates the change in temperature, radius, (and position) of a particle, and the local ambient values are updated for its new position. It should be noted here that the microphysics model for the droplet is essentially that of Andreas (1990) with yet a few minor differences: we have included ventilation coefficients as did Edson and Fairall (1994), and also several of our parameterizations of the above-mentioned parameters are different. In particular, we have paid detailed attention to the osmotic coefficient and surface tension in order to produce a parameterization with the possibility of high salinity. Indeed, when a droplet evaporates, its salinity can dramatically increase. Figure 3 shows the droplet temperature, radius and salinity calculated with this model for a 100-μm droplet with an initial temperature of 22°C and salinity of 34 psu, in air at 20°C and 85% relative humidity. Droplet temperature and radius compare remarkably well with the model of Andreas (1995,his Fig. 1); note that the salinity in this case reaches approximately 185 psu at the droplet radius equilibrium.

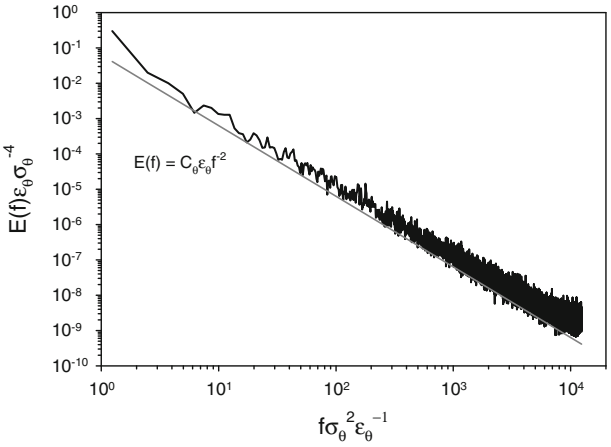

Fig. 4 Spectrum of the carrier fluid temperature following a fluid parcel (*black*) and the theoretical spectrum from scaling analysis (*grey*)

5 Results and Discussion

Over a flat, rigid boundary, Kolmogorov's similarity theory (Kolmogorov 1941, 1962), yields the following Lagrangian time spectrum within the inertial-convective subrange (Inoue 1952; Corrsin 1963):

$$E(f) = C_\theta \varepsilon_\theta f^{-2}. \tag{28}$$

Below the inertial-convective subrange, the spectrum is white, while at frequencies higher than the dissipative frequency scale, the spectrum falls off rapidly in the inertial-diffusive subrange first then in the viscous-diffusive subrange. We have run the model for a fluid particle initially placed at 1 m above the surface in a 15 m s^{-1} wind speed and tracked it as it propagates through the turbulent MBL. The height of this particular droplet never exceeded 30 m above the surface. Figure 4 shows the spectrum for the temperature of a massless fluid particle—the specific humidity case is identical. For comparison, a line proportional to the expected spectrum is also provided. As the particle traverses the MBL and changes height above the surface, the turbulent intensity and the dissipation rate change because they vary vertically in space as do the turbulent fluxes. For the purpose of this comparison and for the results plotted in Fig. 4, we take the mean dissipation rate and turbulent intensity as experienced by the fluid particle as it traverses the MBL. Of course, one advantage of this Lagrangian approach is the ability to follow the heavy particle as it traverses the MBL, which enables a local estimation of various scalars, dissipation rates and other parameters used to solve the particle momentum, heat and mass equations. The modelled spectrum generally follows the expected spectrum but appears to be slightly higher, which could be due to the additional fluctuations from turbulent transport. Also, this could possibly be due to the use of mean values to scale the spectrum. Nevertheless, the temperature spectrum of the fluid parcel still follows the expected frequency dependence. The spectrum continues into the scalar and viscous dissipative subranges due to the timestep requirements that ensure all terms in the exponent of Eq. 22 are small. Although this high frequency fluctuation is not physical, for practical purposes there are no adverse consequences to using smaller timesteps because the variance contained within this range is small compared to the total variance.

In addition, to illustrate the behaviour of the model with heavy, non-fluid particles, we have tracked two different sizes of water droplets as they are transported through the MBL. The heavy particle trajectories were obtained from the model described in Mueller and Veron (2009b), which includes, among other things, the effects of the heavy particle inertia and gravitational settling. Because heavy particles take a finite amount of time to adjust to the ambient airflow conditions, the spectra are expected to depart from the fluid particle case. Moreover, liquid drops not only lose or gain mass through evaporation or condensation but they also lose or gain latent heat. From Eq. 24, there are two distinct terms that determine the droplet temperature. On the right-hand side of Eq. 24, the first term is the sensible heat component, while the second term can be considered the latent heat component. Equation 24 can then be written in the following form:

$$\frac{dT_p}{dt} = -\frac{f_h}{\tau_{SH}}\left(\theta - T_p\right) - \frac{f_w}{\tau_{LH}}\frac{L_v}{\rho c_{ps}}\left(\rho q - q_p\right), \tag{29}$$

where τ_{SH} and τ_{LH} are the time scales respectively associated with the sensible heat and latent heat components:

$$\tau_{SH} = \frac{\rho_p c_{ps} r^2}{3k_a'}, \tag{30}$$

$$\tau_{LH} = \frac{\rho_p r^2}{3\rho K_q'}. \tag{31}$$

As with the molecular fluxes at the air–sea interface, at least with the relatively small temperature gradients typical of the atmospheric marine boundary layer, the latent heat flux component dominates the air-drop heat flux until the droplet reaches and remains at its equilibrium radius. Even though the evaporation time scale is much longer than the thermal time scale, as seen in Fig. 3, which shows that the droplets reach an equilibrium temperature much faster than they reach an equilibrium radius, the time scale of the latent heat flux is close to that of the sensible heat flux. This is physically intuitive (people feel cooler soon after becoming wet even though the water itself takes considerable time to evaporate).

Figure 5a shows the temperature spectrum of a water droplet with 100-μm radius along with the temperature spectrum of the air following the droplet. Because the droplet has significant inertia, its position at each timestep differs from that of a corresponding massless fluid particle. This leads to an additional spatial decorrelation (Eq. 22), and the spectrum of the air temperature following the droplet is somewhat whiter than the case of a fluid particle. The departure is most noticeable at the highest frequencies, where spatial decorrelation is comparable to temporal decorrelation. Nevertheless, this spectrum does not depart substantially, besides being somewhat shallower, from the behaviour expected at the location of a fluid particle. At lower frequencies, the droplet temperature spectrum is higher than that of the air, which means that the droplet temperature fluctuates more than the air temperature surrounding the droplet. This is because, under these typical atmospheric conditions, the latent heat flux dominates the sensible heat flux, and therefore, the temperature fluctuation of the droplets will be dominated by the fluctuation of ambient humidity around the droplet rather than that of temperature. Furthermore, our model only has one-way coupling such that the droplet does not cool the surrounding air as it evaporates. At higher frequencies there is less droplet temperature fluctuation than in the ambient air. This particular droplet is sufficiently large to have a lag in its response time to thermal forcing. Indeed, the droplet temperature spectrum undergoes transition from an f^{-2} regime to an f^{-4} roughly at the frequency equal to the inverse latent heat time scale.

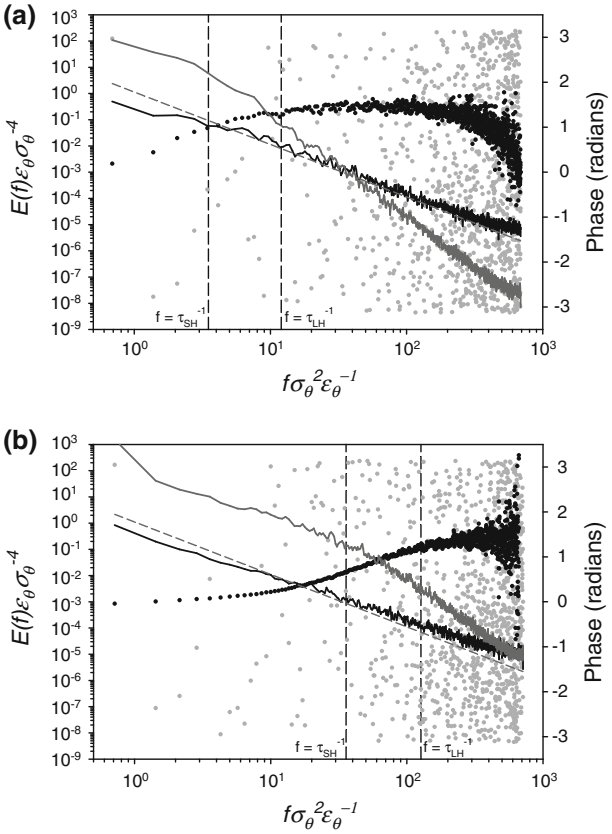

Fig. 5 The temperature spectra of the air following the droplet (*black*) and the droplet itself (*grey*) for a 100-μm radius, water droplet (**a**) and a 30-μm radius water droplet (**b**), along with the theoretical f^{-2} relationship (*dark grey dashed line*) and the phase relationships between the air temperature and droplet (*grey circles*), as well as the specific humidity and the droplet temperature (*black circles*)

The phase relationships between the droplet temperature and the air temperature following the droplet as well as the specific humidity following the droplet are also plotted in Fig. 5a. There is a close phase relationship with ambient humidity that is qualitatively similar to the momentum case (see Mueller and Veron 2009b) even though the phase relationship with ambient temperature is seemingly random. This means that, as stated above, the droplet temperature has a clearer relationship with the ambient humidity than it does with the ambient temperature.

Figure 5b shows the same type of behaviour as Fig. 5a for a water droplet with 30-μm radius. Because the smaller droplet has more surface area relative to its mass and volume, it responds quicker to the ambient conditions. Therefore, the droplet temperature spectrum is generally higher than the temperature spectrum of the air following the droplet for almost all frequencies, even the higher ones. The droplet temperature spectrum only follows an f^{-4} regime at the highest frequencies, i.e. those to the right of the frequency equal to the inverse latent heat time scale. Note that neither droplet stays suspended sufficiently long to reach its equilibrium radius. Speculatively, the phase relationship between the droplet temperature and ambient temperature becomes tighter at extremely low frequencies, which are lower than

those depicted here and where the latent heat relationship may collapse. In the infinite time limit where the radius is in equilibrium, the ambient temperature is expected to dominate the droplet temperature because the latent heat flux is essentially zero when there is no further evaporation or condensation. In this unsteady case, however, the droplet radius can only reach quasi-equilibrium.

Spectral analysis such as the one presented here is useful and ultimately adds insight to some of the particle response to the ambient turbulent conditions, but only so much can be gained from techniques that do not account for local temporal changes. Such limitations arise because the response transfer functions change as the droplets move and evolve. Perhaps a wavelet transform technique, which accounts for temporal changes, would be more appropriate, but it lies beyond the scope of this work. Nonetheless, we feel that this illustrates the strength of Lagrangian techniques with which we can follow droplets as they change and evolve along their flight through the MBL.

Not only does the phase relationship between local specific humidity and droplet temperature look coherent, but the statistical significance of this relationship is also consistently high. Analogous to time-lagged correlations in temporal space, coherence squared values show the significance of correlations in frequency space. Figure 6a and b plot the coherence squared between the droplet temperature and both local humidity and local air temperature for the 100-μm radius droplet and 30-μm radius droplet, respectively. For the middle frequency range, the coherence squared values of droplet temperature with humidity approach 1, while at extremely low and high frequencies, the values decrease fairly rapidly. At the higher end, this roll-off occurs at the frequency equal to the inverse latent heat time scale. There is no identifiable frequency for the decrease in the coherence at the low frequencies.

The statistical significance of the relationship between the droplet temperature and the air temperature is quite low, generally with coherence squared values under 0.5. Again, although the evaporation time scale is relatively large in the steady state case (seen in Fig. 3), the latent heat flux affects the droplet temperature at much smaller time scales or higher frequencies. Analogous to the interfacial heat flux, the latent heat flux appears to dominate the total droplet heat flux at most frequencies. This relationship is particularly important considering that the near-surface humidity is always high, regardless of stratification. In other words, significant warming of falling droplets near the surface occurs at short time scales due to condensation. Even though the droplet radius may not change rapidly, the droplet temperature, due to evaporation and condensation, does.

The next logical step would be to compare the relationship between the droplet radius (or mass) with the ambient air temperature and specific humidity. Unfortunately, such an analysis is not as straightforward and will not be presented here due to the following reasons: first, Eq. 23 does not contain simple analytical solutions for the relative time scales. Second, because the evaporation process occurs over long time intervals, essentially every droplet, without artificial forcing, falls back into the ocean before the evaporation process is complete. Finally, looking at the relevant coherence squared values, there are no distinct time scales for the radius and ambient conditions. At high frequencies, the droplet radius has coherence squared values under 0.5 for both air temperature and ambient humidity. At the lowest resolved frequencies, the coherence squared values go toward 1 between the droplet radius and both air temperature and humidity. Such different behaviour should not be unexpected, as the radius evolution equation (Eq. 23) looks very different from the thermal (and momentum) evolution equation (Eq. 24).

As mentioned above, the model in its current form includes only one-way coupling. The air affects the drops, but the drops do not affect the air so that the air surrounding a droplet does not gain/lose heat or gain/lose moisture as the droplet temperature and radius evolve

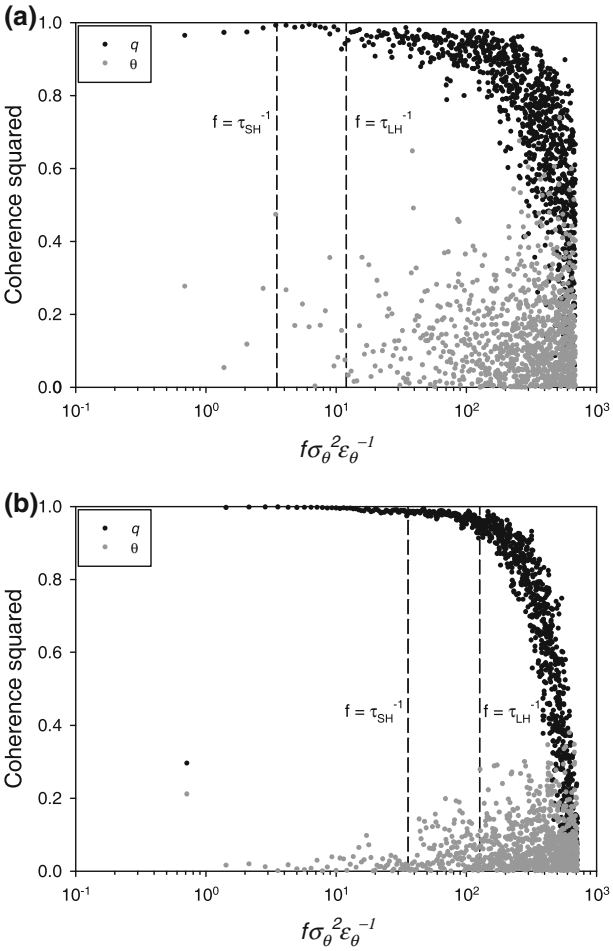

Fig. 6 The coherence squared between the droplet temperature and local air temperature (*grey circles*) as well as that between droplet temperature and local specific humidity (*black circles*) for water droplets with a radius of 100 μm (**a**) and 30 μm (**b**)

during its flight in the near-surface atmospheric boundary layer. In other words, the effects of the droplet evaporation do not modify the mean profiles (Eq. 4) nor do they allow for adjustment of the flux tensors (Eqs. 10–13). Another limitation of the model is that the droplets are independent of each other and thus do not interact, although estimates show that this is not an issue in all but the most highest wind speeds and spray loading conditions.

Despite the limitations of the one-way coupling, arguably, spray mediated fluxes obtained with this model should provide upper bound values because the inclusion of feedback effects would intuitively reduce the spray fluxes. For example, when a drop exchanges heat with the near-surface atmosphere, the air warms and its temperature becomes closer to that of the sea and the drop's initial temperature. This would reduce not only the spray mediated fluxes but also the heat exchanges at the air–sea interface. In its current form, the model presented here is a necessary first step, providing one of many modules that are essential for a comprehensive model of spray mediated fluxes. Accordingly, the inclusion of

feedback mechanisms is currently being developed for subsequent Lagrangian stochastic model runs. Finally, a Lagrangian–Eulerian hybrid model may become routine as computing power increases; in such a model, two-way coupling between the drops and the atmosphere would be explicit at each timestep and grid point, and drop–drop interactions (e.g. collisions) could be implemented naturally.

6 Conclusion

We have developed a Lagrangian stochastic (LS) model for heavy particles in the marine boundary layer (MBL) where the turbulent scalar fluxes of temperature and water vapour change with height above the wavy water surface. In addition to a model for these turbulent fluxes, the traditional LS model has been extended to conserve the second-order, one-point correlations (variances and covariances) and also takes into account the anisotropic, unsteady case. The scalar turbulence of a fluid particle in a Lagrangian frame of reference in the MBL is characteristically similar to the corresponding isotropic case, that is the scalar spectrum still follows rather closely to the predicted inertial-convective behaviour with a f^{-2} dependence. The slight difference observed in the MBL is perhaps a consequence of the additional wave-induced fluctuations from turbulent transport, but the necessity to scale with the mean turbulent intensity and dissipation rate obscures this conclusion.

Along the pathline of a heavy sea-spray droplet, however, the air temperature spectrum no longer follows the theoretical f^{-2} slope. Instead, the actual spectral slope is whiter due to additional decorrelation from the separation between the fluid flow and the particle trajectory. The spectrum of the particle temperature exhibits different regimes. At lower frequencies, where the temperature fluctuation of the droplet is dominated by the fluctuation of ambient humidity around the droplet rather than that of temperature, the droplet temperature spectrum shows a f^{-2} slope at a level higher than the spectrum of the surrounding air temperature. At higher frequencies there is less droplet temperature fluctuation than in the ambient air. The droplet has a lag in its response time to thermal forcing, and the droplet temperature spectrum undergoes transition from an f^{-2} regime to an f^{-4} regime at approximately the frequency equal to the inverse latent heat time scale. Concurrently, the phase relationship between spray temperature and ambient humidity undergoes transition from being in phase to completely out of phase (in quadrature), but the phase relationship between spray temperature and ambient temperature is seemingly random.

We believe that this improved LS model will prove useful in modelling the sea-spray evaporation in the atmospheric boundary layer above a wavy water surface. The Lagrangian approach simplifies the estimation of latent heat and sensible heat fluxes on a *per-droplet* basis, which will in turn assist with the accurate estimate of the overall spray-mediated air–sea fluxes.

Acknowledgements This work was supported by the Office of Naval Research (ONR) under grant N00014-05-1-0609 to Veron. We thank an anonymous reviewer for comments that significantly improved the manuscript.

References

Andreas EL (1990) Time constants for the evolution of sea spray droplets. Tellus B 42(5):481–497
Andreas EL (1995) The temperature of evaporating sea spray droplets. J Atmos Sci 52(7):852–862
Corrsin S (1963) Estimates of the relations between Eulerian and Lagrangian scales in large Reynolds number turbulence. J Atmos Sci 20:115–119

Couzinet A (2008) Approche PDF jointe fluide-particule pour la modelisation des ecoulements turbulents diphasiques anisothermes. PhD dissertation, LInstitut National Polytechnique de Toulouse, 185 pp
Du S, Sawford BL, Wilson JD, Wilson DJ (1995) Estimation of the Kolmogorov constant (C_0) for the Lagrangian structure function, using a second-order Lagrangian stochastic model of grid turbulence. Phys Fluids 7:3083–3090
Edson JB, Fairall CW (1994) Spray droplet modeling. 1. Lagrangian model simulation of the turbulent transport of evaporating droplets. J Geophys Res 99(C12):25295–25311
Edson JB, Fairall CW (1998) Similarity relationships in the marine atmospheric surface layer for terms in the tke and scalar variance budgets. J Atmos Sci 55:2311–2328
Elfouhaily T, Chapron B, Katsaros K, Vandemark D (1997) A unified directional spectrum for long and short wind-driven waves. J Geophys Res 102:15781–15796
Inoue E (1952) On the Lagrangian correlation coefficient of turbulent diffusion and its application to atmospheric diffusion phenomena. Geophys Res Pap No 19:397–412
Kolmogorov AN (1941) The local structure of turbulence in incompressible viscous fluid for very large Reynolds numbers. CR Dokl Acad Sci URSS 30:301–305
Kolmogorov AN (1962) A refinement of previous hypotheses concerning the local structure of turbulence in a viscous incompressible fluid at high Reynolds number. J Fluid Mech 13:82–85
Liu WT, Katsaros KB, Businger JA (1979) Bulk parameterization of air–sea exchanges of heat and water-vapor including the molecular contraints at the interface. J Atmos Sci 36(9):1722–1735
Moissette S, Oesterle B, Boulet P (2001) Temperature fluctuations of discrete particles in a homogenous turbulent flow: a lagrangian model. Int J Heat Fluid Flow 22:220–226
Mueller JA, Veron F (2009a) Nonlinear formulation of the bulk surface stress over breaking waves: feedback mechanisms from air-flow separation. Boundary-Layer Meteorol. doi:10.1007/s10546-008-9334-6
Mueller JA, Veron F (2009b) A Lagrangian stochastic model for heavy particle dispersion in the atmospheric marine boundary layer. Boundary-Layer Meteorol. doi:10.1007/s10546-008-9340-8
Mueller JA, Veron F (2009c) Bulk formulation of the heat and water vapor fluxes at the air–sea interface including nonmolecular contributions. J Atmos Sci 67(1):234–247
Rodean HC (1996) Stochastic Lagrangian models of turbulent diffusion. American Meteorological Society, Boston, 84 pp
Taylor GI (1921) Diffusion by continuous movements. Proc London Math Soc Ser 2 20:196–212
Thomson DJ (1987) Criteria for the selection of stochastic models of particle trajectories in turbulent flows. J Fluid Mech 180:529–556
van Driest ER (1956) On turbulent flow near a wall. J Aeronaut Sci 23:1007–1011
Yeung PK (2002) Lagrangian investigations of turbulence. Annu Rev Fluid Mech 34:115–142